A seismic proxy identifying the transition to an ice sheet polar regime from the sedimentary sequence on the Antarctic continental margin.

Giuliano Brancolini[a]*, Laura De Santis[a], Davide Gei[a], Robert McKay[b], Boo-Keun Khim[c], Carlota Escutia[d], Giuseppe Brancatelli[a], Riccardo Geletti[a]

[a]*National Institute of Oceanography and Applied Geophysics (OGS), 34010 Sgonico TS, Italy*
[b]*Antarctic Research Centre, Victoria University of Wellington, Wellington 6012, New Zealand*
[c]*Department of Oceanography, Pusan National University, Busan 46241, Republic of Korea*
[d]*Instituto Andaluz de Ciencias de la Tierra CSIC , Univ. de Granada, Armilla (Granada), Avda de las Palmeras 4 18100, Spain*

*Corresponding author
E-Mail address: giuliano.brancolini@gmail.com (G. Brancolini)

ABSTRACT

Based on the integrated analyses of seismic and borehole data from the Antarctic continental shelf and rise in the offshore area of Wilkes Subglacial Basin, we recognize two major turning points in the evolution of the East Antarctic Ice Sheet: in the early Miocene and early Pliocene, defined by the establishment and deactivation of a noticeable channel-levee system on the continental rise. Our observation supports the earlier hypothesis that ice volume increased nonlinearly with climate during the Miocene Climatic Optimum (17-14.8 Ma), the warmest period of the Neogene, as a result of high snowfall under humid climatic conditions with high moisture supply onto a more terrestrial landmass prior to extensive erosion and overdeepening of Antarctica's continental shelves. The deactivation of the channel-levee system, evidenced by the progressive filling of the channels on the rise and the deposition of steeply dipping foreset beds at the shelf margin, occurred at about 3.3 Ma, at the end of the early Pliocene warm period, and represents the transition to the present polar regime. The late Miocene and the early Pliocene are also characterized by a particular high-amplitude seismic facies that is the signature of alternating terrigenous and diatom-rich layers representing glacial and interglacial periods. This facies characterizes the upper part of the channel system and may represent a new significant environmental and stratigraphic marker, particularly for the early Pliocene warm period elsewhere along the Antarctic continental margin.

Keywords: Antarctica, ice sheet, Wilkes Basin, IODP Leg 318, seismic facies, diatoms.

1. Introduction

Coupled atmosphere-ocean general circulation models (GCMs) are often used to predict the scenario of future global warming (e.g., Siegert and Golledge, 2022). However, the conclusions of the models are highly dependent on the assessment of climate drivers and boundary conditions, one of which is the volume and thermal regime of the Antarctic Ice Sheet (AIS) (e.g. Pollard et al., 2015; Colleoni et al., 2018; Albrecht et al., 2020). Considering the difficulties in parameterizing all variables, the robustness of the numerical models largely depends on benchmarks based on past AIS configurations.

The Neogene represents the transition of the Earth's climate from the "coolhouse" to the current "icehouse" state (Westerhold et al., 2020). This period includes several critical steps in AIS history (Levy et al., 2022; Colleoni et al., 2022 for a comprehensive overview), such as the Miocene Climatic Optimum (MCO), the Middle Miocene Climatic Transition (MMCT), the Late Miocene Cooling (LMC) and the Pliocene Warm Period (PWP). The warmer periods (MCO and PWP) of the Neogene, in particular, are attracting great attention as possible analogies for future global warming.

The MCO (*ca*. 17-14.8 Ma) was the warmest period of the last 35 Ma, with average Bottom Water Temperatures (BWT) of 3°-9°C higher than today (Steinthorsdottir et al., 2021; Modestou et al., 2020; Billups and Schrag, 2003; Lear et al., 2015) and atmospheric CO_2 concentrations between 400 and 600 ppm (Cui et al., 2020; Sosdian et al., 2018; Zhang et al., 2013). After the MCO, during the MMCT (*ca*. 14.8-13.8 Ma), there was a rapid deterioration of the global climate (Zachos et al., 2001; Shevenell et al., 2004), with BWT dropping by up to 4°C (Lear et al., 2015; Shevenell et al., 2008; Cramer et al., 2011) and CO_2 levels falling below 300 ppm (Badger et al., 2013; Holborun et al., 2013). For these aspects, the MMCT has been considered an ecological tipping point (Levy et al., 2022), with significant growth of the AIS (Flower and Kennett, 1994; Westerhold et al., 2020; Pierce et al., 2017), the possible establishment of an ice sheet in the Northern Hemisphere and a reorganisation of polar fronts (Kuhnert et al., 2009; Verducci et al., 2009; Holbourn et al., 2013; Wen et al., 2023). Another more moderate cooling, the LMC, characterized the late Miocene, with a decrease in BWT of about 2°C in the Southern Ocean and an increase in temperature gradients in the South Pacific (Herbert et al., 2016; Zhang et al., 2013; Cramer et al., 2011).

The MCO was followed by a subsequent climatic warming of lower magnitude (the PWP) in the early Pliocene. The PWP is the best-studied period of the Neogene, as it was the last time in Earth’s history when atmospheric CO_2 concentrations (*ca*. 400 ppm) were similar to today and global mean sea surface temperatures were 2°-3°C warmer than today (Haywood and Valdes, 2004; Lunt et al, 2010; Martínez-Botí et al, 2015; Raymo et al, 1996). The cooling after the PWP led to today's “icehouse” conditions with a polar regime in Antarctica and the onset of intensive glaciations in the Northern Hemisphere (De Boer et al., 2010; Mudelsee and Raymo, 2005; Bartoli et al., 2011).

With an ice volume of 3-4 m sea level equivalent, the Wilkes Subglacial Basin (WSB) is the largest low-lying East Antarctic basin and a critical area for the stability of the East Antarctic Ice Sheet (EAIS). Due to the landward deepening of the basement beneath the ice sheet, the WSB is sensitive to marine ice sheet instability triggered by warm water intrusion from the Southern Ocean (Aitken et al., 2014; Fogwill et al., 2014; Pritchard et al., 2012; Greenbaum et al., 2015; Morlighem et al., 2020). The area off George V Land (Fig. 1) preserves an expanded record of eroded sediment derived from the WSB, which is thought to be regulated largely by shifting ice sheet dynamics through time (Cook et al., 2013; Patterson et al., 2014; Golledge et al., 2021). However, prior to the implementation of Integrated Ocean Drilling Program (IODP) Expedition 318, almost all interpretation were based on seismic data with limited stratigraphic control.

Seismic sequences from the continental margin have been related to the long-term evolution of the ice sheet in the WSB, from the “coolhouse” to the “icehouse” states, according to the Westerhold et al., (2020) definition (Escutia et al., 2005). Uniform, subparallel, low-amplitude, and continuous reflectors represent the preglacial or glacial distal deposits, while the giant channel-levee systems, that have formed perpendicular to the continental shelf since the early Miocene, characterized by discontinuous, mound-shaped and distorted reflectors, have been related to a substantial growth of the ice sheet in a subpolar regime (De Santis et al, 2003; Donda et al, 2003; Close et al, 2007). The sediment waves (Fig. 2a) that formed on the channel levees, were interpreted as episodic turbiditic overflow deposits (Donda et al., 2007). The most recent “icehouse” state (Pliocene? to Recent) is interpreted from semi-transparent, and less continuous reflectors, shaped by a persistent downward bottom water flow on the continental rise and by the development of steep and projecting wedges at the shelf margin (Donda et al., 2007; Escutia et al., 2005). Due to the lack of drilling data, the age of these sequences could only be determined tentatively, with large uncertainties. Here we present a new stratigraphic assessment of the seismic sequences off the WSB, based on a robust time-depth conversion of the seismic data and correlation with the data from IODP Expedition 318.

The IODP Expedition 318 wells penetrated one of the few near continuous Cenozoic sections for the entire Antarctic and represent the long-term record of the sedimentary archives of the WSB glaciations and its intimate relationships with global climatic and oceanographic changes (Escutia et al., 2011a). Sediments from the early Eocene to the late Miocene were found in borehole U1356, but recovery rates were low in many intervals necessitating the integration with seismic data to provide a more complete interpretation of ice dynamics through this period. During the middle to late Miocene, the predominant lithofacies consists of clay-rich diatom oozes and diatom-rich silty clays with scattered gravels, indicating hemipelagic sedimentation with iceberg rafting, although distal turbidite facies (laminated silty clays) increase in the Middle Miocene (Sangiorgi et al., 2018). Palynological and paleontological data from Site U1356 demonstrate that, during the MCO, temperatures in the Wilkes Land area were still high enough (minimum MATs > 5°C) to sustain woody subantarctic vegetation under partially ice-free conditions (Salzmann et al., 2011; Sangiorgi et al., 2018; Crampton et al., 2016; Duncan et al., 2022). After the MCO, during the MMCT, temperatures cooled and the continental cryosphere underwent a large expansion, as evidenced by the large amounts of ice-rafted debris (IRD) deposited in various pulses at Site U1356 between 14.1 and 13.8 Ma (Pierce et al., 2017).

Sediments from the late Miocene to the present were recovered in Holes U1359 and U1361 and can be categorized into two main groups associated with the retreat and growth of the EAIS (Khim et al., 2017; Escutia et al., 2011b): i) laminated mud with low biogenic opal content (less than 10%), representing overbank turbiditic deposits during the glacial period, ii) massive mud with high biogenic opal content (30-50%), representing hemipelagic and contouritic deposits during the interglacials (Cook et al., 2013; Patterson et al., 2014). Detailed studies on the two sites have focused pretty much exclusively on the PWP (Bertram et al., 2018; Armbrecht et al., 2018; Patterson et al., 2014). In particular, Taylor-Sylva et al. (2018) used the diatom record from U1361 to demonstrate that the increasingly sea-ice-influenced environment in the late Pliocene was punctuated by at least a single interglacial in which the Antarctic polar front moved strongly southward, while the increased dynamic discharge of the ice sheet occurred during the PWP, with its retreat of several hundred kilometres within the WSB, were supported by the origin and accumulation rates of glacimarine muds and IRD (Cook et al., 2013; Patterson et al., 2014).

Hole U1358 was drilled on the continental shelf and, despite its shallow penetration depth (*ca*. 35 m) and poor recovery (*ca*. 20%), contains a useful early Pliocene record whereby periods of open-marine conditions with glaciomarine sedimentation punctuated by at least four extensive glacial advances (Reinardy et al., 2015; Orejola et al., 2014).

In this paper, we integrate seismic and IODP data from the continental shelf and the rise off George V Land (Fig. 1) and propose a model for the Neogene long-term glacial history of the WSB. We have also identified a particular high-amplitude seismic package (HASP) that represents the alternation of diatom-rich and terrigenous-rich strata that marks the transition to a less erosive and dynamic EAIS during the late Pliocene. The possibility of using this seismic facies as a paleoecological or stratigraphic marker elsewhere is interesting, but requires further analysis of similar areas in Antarctica.

2. Methods

Our study is based on the integrated analyses of multichannel reflection seismic and borehole data, stratigraphy and logs, from IODP Expedition 318, sites U1359, U1361, and U1358 (Escutia et al., 2011b). The method we used consists of three steps: seismic data reprocessing, seismic borehole coupling and petrophysical characterization.

2.1. Reprocessing of seismic data

The first step was the reprocessing of part of the multi-channel seismic profiles recorded in February/March 2000 by the R.V. *Tangaroa* (Brancolini and Harris, 2000) as part of the Australian-Italian WEGA project (Table 1).

Source	Streamer length	Min. offset	Num. of traces	Group interval	Shot interval	Fold	Sampling interval
2GI-Gun 6.8 l	500 m	170 m	40	12.5 m	25 m	10	1 ms

Table 1: Acquisition parameters of the WEGA seismic lines.

The aim of the reprocessing was the production of real amplitude seismic images that can be properly correlated to the well log data at Sites U1359 and U1361. The main steps in the reprocessing were: bandpass filtering (3/7-140/150 Hz), time resampling from 1 to 2 ms, data editing, amplitude decay recovery, CMP (common mid-point) sorting, velocity analysis, normal move out correction, CMP stacking, and frequency-wavenumber time migration.

The challenge was to restore the amplitude decay. Amplitude decay of seismic data is mainly due to spherical divergence, frequency absorption, and transmission losses. These parameters cannot be determined analytically (Ylmaz, 2001). To overcome this problem, seismic data are usually processed by applying automatic gain control or window balancing. Both methods are useful to emphasize weak signals, but change the signal character so that strong reflections can no longer be distinguished from weak reflections and some of the geophysical information are lost. To avoid this, we applied only an empirically defined exponential function to the data, which, despite the poor visibility of the weaker reflections in the deeper part of the sections (Fig. 2b, 2c, and 2d), reproduces the seismic data with their actual amplitude. The most prominent feature in all reprocessed sections (Fig. 2b ,2c, and 2d) is the presence of an high amplitude seismic package (HASP) defined by the unconformities WL-U8a and WL-U7, which has a variable thickness between 100 and 300 ms, corresponding to about 80-250 m. For comparison, we show a window-equalized version of the seismic line (Fig. 2a and 2b). In Fig. 2a, the geometry of the channel system reflectors can be seen more clearly, but the differences in seismic amplitude anomalies are not readily apparent.

2.2. Seismic borehole coupling

The link between seismic and borehole data was established by calculating a synthetic trace from the density and sonic logs. Where available, we used the wireline data rather than the multi-sensor logger (WRMSL) data. This is because the wireline data are continuous and represents *in situ* measurement, whereas WRMSL data are core laboratory measurements that generally differ from *in situ* values due to sediment decompaction and discontinuity of recovery. We used WRMSL data only to integrate the uppermost part (above 100 m) of the sediment section for which no wireline logs are available (see Gei et al., 2024 for further explanation and references).

Four holes were drilled at Site U1359, with downhole logging conducted only in Hole U1359D in the approximate depth range of 104–602 mbsf. Two holes were drilled at Site U1361 and downhole logging was conducted in Hole U1361A from 103-388 mbsf-meter below sea floor. Based on the continuous velocity and density profiles from the seafloor to the bottom of the borehole, obtained by integrating the wireline and WRMSL data, we calculated the acoustic impedance and reflection coefficient for the entire borehole sections (Fig. 3). The synthetic trace in the time domain was obtained by convolving the reflection coefficient with the wavelet extracted from the seafloor reflection near the borehole (Gei et al., 2024). In Fig. 3, the synthetic trace (green) is compared with the real trace (red) and shows a fairly good correlation, particularly for the HASP, where the correlation coefficient is about 0.80. That indicates that the HASP is not a seismic artifact but a petrophysical property of the sediment.

Reliable velocity functions, required to link seismic and borehole data, in our case cannot be derived from seismic velocity analysis because the length of the streamer (500 m) was short compared to the depth of the targets (about 3000 mbsl – meters below sea level). Consequently, the conversion from depth to time was made using the velocity function obtained by integrating the sonic logs from boreholes and cores. We are quite confident about the results of our method because the link between seismic and borehole was refined by correlating the synthetic traces with the seismic data near the boreholes and stretching and compressing the synthetic data with a Time Variant Cross-correlation method (Gei et al., 2024; Cui and Margrave, 2015). We check the reliability of the applied time shifts by calculating the updated local velocities, obtaining a maximum velocity perturbation of 5%.

2.3. Petrophysical characterization

The sedimentary sequences at Sites U1359 and U1361 are predominately characterized by two end members: diatom-rich (biogenic opal >30%) silty clay with abundant bioturbation and planar laminated silty clay (biogenic opal <10 %). These two types of deposits are associated with reduced sea-ice coverage and ice-sheet retreat during interglacial periods and sea-ice extent and ice-sheet growth during glacial periods, respectively (Escutia et al., 2011b; Khim et al., 2017).

Fig. 4a shows a biogenic opal log combining the results of Khim al. (2017) for the Pliocene section with new analyses of the entire cored section. Core recovery at the two sites was quite good (60% at Site U1359D and 87% at Site U1361), nevertheless, there are significant gaps in the lithologic logs that affect the continuity of the logs and depth determination. We addressed the problem by merging the biogenic opal logs (Fig. 4a) with the natural gamma ray (NGR, Fig. 4b) and density (D, Fig. 4c) logs from wireline and core measurements (Escutia et al., 2011b). Diatoms, which are the main component of the biogenic opal content in the sediments here, are not radioactive and dilute the NGR signal of the terrigenous minerals, while the density variability is due to the lower grain density of the diatoms (2.20 g/cm^3) compared to the higher (2.80 g/cm^3) of the silty clay layers (Awadalkarim et al., 2014; Khim al., 2017; Escutia et al., 2011b). Fig. 4 shows that high NGR and density values correspond to silty-clay units, while low NGR and density values correspond to diatom-rich massive mud. For the uppermost 100 m of the two boreholes for which no wireline logs are available, we used the WRMSL data. The NGR units differ between the WRMSL and wireline logs, and to create a continuous log, we arbitrarily shifted the WRMSL data to match the gAPI scale of the wireline log. In addition, the core and WRMSL data were shifted by approximately 5 m to compensate for a discrepancy between the depths of the wireline and cores

3. Results

Based on the seismic and borehole coupling, we defined the depth of the main seismic unconformities in the study area. The results are summarized in Table 1, where the age estimates are based on the magnetic reversals and biostratigraphy of Tauxe et al. 2012 and illustrated in Fig. 5. The velocity functions we adopted at the well sites are about 20% lower than the functions adopted by Escutia et al. (2011b), consequently, our depth estimates are shallower than previously evaluated by Escutia et al. (2011b). In addition to previous unconformities (De Santis et al., 2003), we introduced the new WL-U8a (3.3 Ma) and WL-U7a (6.2 Ma). WL-U8a define the upper boundary of the HASP while the base is diachronous and its first appearance correspond to WL-U7 in the upper rise, at Site U1359, and to WL-U7a at site U-1361 (Fig. 2a). The correspondence between the age of the unconformities at the two sites, resulting from the age-depth plot, confirms the validity of the seismic correlation between the two sites.

	Site U1359		**Site U1361**		
Unconformities	***Time (ms)***	***Depth (mbsf)***	***Time (ms)***	***Depth (mbsf)***	***Age (Ma)***
WL-U8a	*4170*	*70*	*4770*	*75*	*3.3*
WL-U8	*4230*	*115*	*4820*	*111*	*4.6*
WL-U7a	*4320*	*192*	*4870*	*150*	*6.2*
W-U7	*4400*	*253*	*4980*	*238*	*9.0*
WL-U6	*4780*	*580*	*5200*	*--*	*13.0*

Table 2 Time, depth and ages for the main unconformities based on well and geophysical data. Age attribution from the paleomagnetic tie points from Tauxe et al. 2012

The oldest seismic sequence sampled in Holes U1359 and U1361 is WL-S7 (Fig. 2), between unconformities WL-U6 and WL-U7. WL-U6 was reached near the bottom of Hole U1359 at about 580 mbsf and has an estimate age of 13.0 Ma, whereas borehole U1361 ends about 50 m above WL-U6. At Site U1359, this depth in WL-U6 corresponds to a limestone that was captured at the bottom and top of successive core runs, and although poorly recovered it is potentially ~6m thick. This limestone bed separated laminated silty clay packages, and the large positive velocity and density peak at this depth supports our interpretation that this bed is more substantial than the few centimetres of recovered core suggests (Fig. 3).

Using Table 2 we calculated the average deposition rates, uncorrected for compaction, for each seismic sequence (Fig. 5). The deposition rate for the WL-S7a sequence at Site U1359 was corrected because the seismic data indicate that the lower part of WL-S7a is missing at the site due to overburden on the underlying sediment wave (Fig. 2d). Outside the borehole, the thickness of the sequence is about twice as large, giving a more realistic sedimentation rate of 34 m/Ma (Fig. 5).

In both sites, the average deposition rates for the seismic sequences decrease from the oldest (about 40-50 m/Ma), to the most recent (about 20m/Ma), likely due to the progressive decreasing of the turbiditic supply from the continent, consequence of the transition froma dynamic to a more persistent ice sheet and finally to a polar regime, when most sediment delivered to the margin was trapped in the outer shelf and slope,-forming steep prograding wedges. (Escutia et al., 2000, Escutia et al., 2002).

In the biogenic opal logs of Fig. 4a, the vertical dashed lines mark the diatom-rich (more than 30% biogenic opal content) and silty-clay (less than 10% biogenic opal content) fields. By integrating these data with the NGR and density logs (Fig. 4b and 4c), we obtained a comprehensive log of diatom content in the two boreholes (Fig. 4d). The integration was based on the following criteria: Above 300 m, the diatom content is derived from the agreement of the three logs according to the above criteria. Below 300 m, where recovery is particularly poor for Site U1359 and diagenetic processes reduce the variability of density, the biogenic opal content was determined mainly from the NGR data.

Fig. 4 shows the remarkable correspondence between the HASP and the diatom content evaluated from the logs integration at Sites U1359 and U1361 (Fig. 5d). This is not surprising as the density variability, as a result of the diatom concentration, strongly influences the acoustic impedance (see Fig. 3) and causes the observed seismic amplitude anomalies.

4. Discussion

The formation of the channel-levee system on the continental rise, postdated the WL-U5 seismic unconformity (Figs. 2a and 2d). WL-U5 was not reached by IODP sites drilled directly to George V Land (e.g. Sites U1359 and U1361) and therefore has not been dated but, based on the extrapolation of sedimentation rates at Sites U1359 and U1361 to the sediment above WLU5, its age can be estimated between ~17 and ~22 Ma. This is consistent with the age of WL-U5 at IODP Site U1356, located a few hundred kilometres west of Sites U1361 and U1359, where WL-U5 corresponds to a hiatus between 17.5 and 24.3 Ma (Escutia et al., 2011b).

According to previous studies (Escutia et al., 2000; Escutia et al., 2002; De Santis et al., 2003, Escutia et al., 2005), we consider the growth of the channels-levees system above the tabular sedimentary deposits, as evidence of the expansion and dynamic of the ice sheet over the WSB, which eroded sediments from the interior and transported them to the continental margin.

Based on the age estimates for WL-U5, the ice sheet expansion occurred in the early Miocene, before the MCO, and may correspond to the Mi-1 event (Escutia et al., 2014; Salabamada et al., 2018; Hartman et al., 2018). As the ice sheet expanded and calved into the sea during glacial periods, the channel-levees grew, as also evidenced by the presence and distribution of IRD from Holes U1359, U1361, and U1356 (Escutia et al., 2011b; Patterson et al., 2014; Pierce et al., 2017) and by the sedimentation on the continental rise, which mainly consists of turbiditic, diatom-poor, laminated deposits (lithologic facies 3-5 from Escutia et al., 2011b). During the warm periods, the ice sheet retreated inland and hemipelagic, massive, bioturbated, diatom-rich sedimentation occurred on the continental rise (lithological facies 1 and 2 from Escutia et al., 2011b).

The early Miocene settlement of the channel-levee system and its growth throughout the MCO, the warmest period of the Neogene (WL-S6 in Fig 2 and 6), seems contradict the widespread attribution of a relevant growth of the EAIS to the MMCT (Levy et al., 2022; Flower and Kennett, 1994; Westerhold et al., 2020; Pierce et al., 2017). A possible explanation is that our age assignment is not correct, resulting that WL-U5 is 3-4 Ma younger and coincides with the MMCT. This is possible because of the correlation with the seismic profiles from Site U1356 to U1361 over a long distance. However, the seismic unconformity of 17-23 Ma at Site U1356 is the base of the channel levee systems (Donda et al., 2007). Furthermore, a younger age for WL-U5 implies a sedimentation rate below U1359 of about 150 m/Ma and of 90 m/Ma below U1361. This is unlikely as it would double the sedimentation rate of the overlying, mainly turbiditic sequence.

An alternative hypothesis to explain the large sediment input to the continental slope at the beginning of the MCO warm period is that the growth of the ice sheet at this time was a consequence of the high moisture input to Antarctica and ice accumulation during the glacial periods (Prentice and Mattius, 1991). This model was also proposed by Shevenell et al. (2008) to reconcile the Southern Ocean temperatures from Mg/Ca records and δ^{18}O ice volume, and is supported by the relative seal level variations from the New Jersey continental shelf (Kominz et al., 2016) and the Marion Plateau (Fig. 6), which show that AIS volume during the glacial of MCO was at least 90% of present-day volume, with variations of up to 60% (John et al., 2011).

Geochemical, petrographic, and geophysical data from the Antarctic continental margins also show large fluctuations in AIS volume prior to, and during the MCO (McKay et al., 2022 and references therein). In the Ross Sea, ANDRILL (Site AND-2A) cores and inland records from the Transantarctic Mountains show that the ice sheet margins retreated inland towards the Transantarctic Mountains during the warmest MCO intervals, when tundra vegetation dominated the ice-free areas (Lewis et al., 2007; Levy et al., 2016; Perez et al, 2022; Chorley et al., 2023), while glacial sediments recovered from IODP Site U1521 suggest that marine terminating ice sheets were absent during peak warmth of the MCO, but during colder glacial intervals prior to, and within the MCO extended into the Ross Sea basins, depositing massive and layered diamicton over a shallow continental shelf (Marschalek et al., 2021; McKay et al., 2025; Bombard et al., 2024).

We hypothesize that a similar environment characterized the WSB during the MCO warm periods, the retreat of EAIS ice margin, allowed seawater to penetrate far inland and vegetation to grow in the ice-free zone (Sangiorgi et al., 2018). On the continental rise, terrigenous supply was scarce and hemipelagic deposits dominated. During the colder orbital and climate states within the MCO interval, glacial periods were still comparatively warmer compared to post MMCT states, resulting in high rates of snow precipitation, and reduced surface melt rates (Hartman et al., 2018). This led to ice sheet accumulation on terrestrial hinterland of East Antarctica and advance of this ice into shallow water areas of the continental shelf adjacent to the WSB. Similar to what has been recently observed in the Ross Sea (McKay et al., 2025), this led to an expansion of the ice sheet, eroding the interior and transporting sediments to the continental margin. The sedimentary response to this large variability of ice volume in the MCO is displayed by enhanced turbiditic flow on the continental rise, creating the channel and surface system depicted on the seismic data (Fig. 2). This model is also supported by numerical simulations (Paxman et al., 2020).

The seismic and geologic data show that the channel-levee system continued to grow up to the end of MMCT climate cooling, corresponding to the WL-U6 seismic unconformity (Fig. 2). After WL-U6 the channel-levee system remained stable, during a relatively stable period of bottom water temperature and $\delta^{18}O$ values (Fig. 6), with glacial sediment supply from the continent on the continental rise.

The upper part of the channel-levee system is characterized by the high amplitude acoustic facies, we termed HASP, between WL-U7 (9 Ma) and WL-U8a (3.3 Ma). During this period, the relative sea-level fluctuations, deep-sea benthic $\delta^{18}O$ and $\delta^{13}C$ curves and seafloor temperatures (Fig. 6) indicate periodic growth and decay of the Antarctic ice sheet, as the Northern Hemisphere ice sheets were not yet fully developed (Westerhold et al., 2020). The HASP time interval spans two important climatic periods: Late Miocene Cooling (LMC) and Pliocene Warm Period (PWP, Fig. 6) but does not appear to be the expression of a specific climatic interval. The sediments corresponding to the HASP at Sites U1359 and U1361 are similar to the underlying sequences with meter-scale variability between alternating intervals of bioturbated silty clays and massive or laminated diatom-rich silty clays (Escutia et al., 2011b). However, in the HASP, the diatom content during interglacial periods is persistently higher and shows greater variability (Fig. 4), which, together with the variability of the IRD, indicates large environmental fluctuations probably related to the advance of the ice sheet and subsequent massive calving of the ice during deglacials and long sea-ice-free periods during interglacials (Cook et al., 2013; Patterson et al., 2014; Bertram et al., 2018). In this case, the seismic facies appear to be an indirect indication of the glacial dynamics of the marine-based ice sheet in the WSB.

It is also interesting that the age of the HASP coincides with the Late Miocene Biogenic Bloom (Dickens and Owen 1999, Pillot 2023). There is no evidence in the literature of a biogenic bloom around Antarctica during this same time interval, although Antarctic sites are underrepresented as only two sites were analyzed by Pillot et al. (2023) and IODP 318 Sites were not included. Detailed analyses of diatom accumulation rates at Sites U1359 and U1361 would therefore be necessary to confirm the presence of late Miocene biogenic blooms off Wilkes Basin in this time interval. The HASP is a particular acoustic facies identified throughout the seismic grid that preserves the geologic record deposited during the transition to the present-day polar regime that emerged at the end of the warm PWP. This is the first time that this seismic facies has been identified, and we suggest that further analysis of drilling and seismic data would be important to verify the potential of the HASP as a paleoenvironmental and stratigraphic proxy elsewhere.

After WL-U8a (3.3 Ma), seismic facies show the filling and dropping of the previous channel-plane morphology (Fig. 2). This change indicates a gradual decrease in sediment supply from the continent to deep water, which is consistent with the decrease in sedimentation rates observed at Sites U1359 and U1361 (Fig. 5). A notable change in seismic sequence geometry above and below WL-U8a can also be observed on the continental shelf (Fig. 7a), from what was previously described as Type IIA to Type IA (Cooper et al., 1991). Type IIA sequence consists of alternating aggradational and progradational seismic reflectors and is interpreted as reflecting changes in sediment accommodation space caused by the interaction of sea level, tectonic, and glacial processes. Type IA sequence consists mainly of prograding reflectors with steep continental dip (up to 12°), which are eroded at the top and are interpreted as a sign of the prevailing processes of a thick ice sheet at the continental margin. During the deposition of Type IA seismic sequence above WL-U8a, the continental margin shifted seaward by about 30 km, filling in the former slope canyons (Fig. 7b).

The strong seafloor prevents the direct correlation of seismic reflectors from the continental margin to the shelf, but a reliable reconstruction of the shelf margin correlation based on Site U1358 is proposed for the youngest sequences. This site penetrates only 35.6 mbsf deep and has a

22% recovery consisting mainly of glacial diamicton. Diatom stratigraphy provides a tentative Pliocene age for most of the section, with most ages older than 2.54 Ma (Escutia et al., 2011b), but the lower section of the core dates to 4.2–5.12 Ma (Reinardy et al., 2015). In agreement with previous studies (Escutia et al., 2011b), we consider WL-U8 (4.6 Ma) to be the unconformity located at approximately 80 m below the seafloor at Site U1358 (Fig. 7a), whereas the younger WL-U8a (3.3 Ma) correlates with the unconformity at 9 mbsf described by Orejola et al. (2014) as marking a change in sediment provenance and ice sheet regime. We hypothesize that WL-U8a marks the boundary between the mostly aggradational Type IIA sequences and the mostly progradational Type IA sequences. The glaciomarine sediments below this hiatus at Site U1358 have been interpreted to be deposited in the Lower Pliocene (Escutia et al., 2011b), under environmental conditions consistent with the alternation of retreating ice margin and high sea surface temperatures in the Southern Ocean (Whitehead and Bohaty, 2003, Escutia et al., 2009) and an extensive grounded marine-based ice sheet. The diamicton above the hiatus at 9 mbsf at Site U1358 suggests an increase in subglacial transport or ice rafting in a glacimarine environment (Orejola et al., 2014). WL-U8a (Fig. 6) also coincides with a strong change in $\delta^{13}C$ and $\delta^{18}O$ values of benthic foraminifera and a drastic decrease in bottom water temperature and global sea level, marking the transition to the current icehouse climate state with the deposition of Northern Hemisphere ice sheets (Westerhold et al., 2020).

Based on these considerations, we hypothesize that the transition to drier and colder climate resulted in a less dynamic margin of the EAIS in the WSB occurred after WL-U8a. This reduced dynamism, This in turn meant less meltwater at the ice base and thus less sediment erosion in the interior and less transport to the continental margin. The sediments deposited at the bedrock zone were more cohesive and compact, leading to the formation of shelf-edge fans consisting of steep (up to 12°), foreset beds and pinching out at the continental slope (Fig. 7a) and gradually filled the canyon heads that characterize the rise (Fig. 7b). The continental rise was gradually starved, and the reduction of sediment supply from the shelf to the continental rise led to a narrowing of the channel and filling of the former relief, as previously observed (De Santis et al., 2003).

5. Conclusion

In this paper we have presented an integrated study using multichannel seismic drilling, wireline logs and stratigraphic data from IODP Sites U1356, U1358, U1359, and U1361 to reconstruct the evolution of the pre-George V Land area. This area is of particular interest as the glacial history of the WSB has been recorded here, where the EAIS is particularly vulnerable. The studied interval covers a large part of the Neogene and includes two warm periods (the MCO and the PWP), which have been widely studied because they are considered analogues for future global warming scenarios. Our main conclusions are:

1. Deposition of glacial sediments that were redeposited in turbiditic channel-levees in the Antarctic continental rise began about 17-22 Ma, showing a growth of the EAIS over the WSB prior to and potentially during the MCO (i.e., the warmest period of the Neogene). This can be explained by the growth of the ice sheet driven by increasing moisture and ice accumulation in the terrestrial or shallow water areas of Antarctica during the relatively colder glacial periods of the MCO – supporting similar observations in the adjacent Ross Sea. This confirms the earlier hypothesis of a complex non-linear relationship between global temperature and ice sheet volume;
2. The channel-levee complex in the offshore of the WSB grew up to the seismic unconformity WL-U6 (13.0 Ma), roughly corresponding to the end of the MMCT, and remained relatively stable until the seismic unconformity WL-U8a (3.3 Ma), roughly corresponding to the end of the PWP.
3. A large portion of the channel-levee complex, between seismic unconformities WL-U7 (9.9 Ma) and WL-U8a (3.3 Ma) is characterised by the HASP, a distinct high-amplitude seismic facies created by the alternation of terrigenous-rich and diatom-rich strata. The HASP documents a period of remarkable instability of marine based ice sheet in the WSB until 3.3 million years ago. The

disappearance of the HASP marks the transition of the WSB ice sheet from a highly dynamic to a more stable system whereby interglacial-glacial variance was reduced in extent. This is the first time that this seismic facies has been recognized, and it could provide a valuable environmental and stratigraphic marker for other areas of Antarctica if recognized on continental rise seismic sequences.

Acknowledgments

We used the academic licence of the IHS Kingdom software provided to the OGS for the seismic interpretation and the IODP Exp. 318 site plots. This study was supported partly by Korea Institute of Marine Science & Technology of the Ministry of Oceans and Fisheries (RS-2023-00256330; to BKK) and by Italian Program for Antarctic research (PNRA).

Supplementary material

A large scale of figures 1, 2, 3, 4 and 7 is available from supplementary material.

Data availability Seismic data in SEG-Y format can be retrieved from the Seismic Library Data Centre https://scar.org/library-data/data/seismic-data. Well logs data from https://www.iodp.org/

References

Aitken, A. R. A., Young, D. A., Ferraccioli, F., Betts, P. G., Greenbaum, J. S., Richter, T. G., ... & Siegert, M. J., 2014. The subglacial geology of Wilkes land, East Antarctica. Geophysical Research Letters, 41(7), 2390-2400.

Albrecht, T., Winkelmann, R., & Levermann, A., 2020. Glacial-cycle simulations of the Antarctic Ice Sheet with the Parallel Ice Sheet Model (PISM)–Part 2: parameter ensemble analysis. The Cryosphere, 14(2), 633-656.

Armbrecht, L. H., Lowe, V., Escutia, C., Iwai, M., McKay, R., & Armand, L. K., 2018. Variability in diatom and silicoflagellate assemblages during mid-Pliocene glacial-interglacial cycles determined in Hole U1361A of IODP Expedition 318, Antarctic Wilkes Land Margin. Marine Micropaleontology, 139, 28-41.

Awadalkarim, A., Sørensen, M. K., & Fabricius, I. L., 2014. Petrophysical Analysis of Siliceous-Ooze Sediments, Møre Basin, Norwegian Sea. Petrophysics, 55(04), 333-348.

Badger, M. P., Lear, C. H., Pancost, R. D., Foster, G. L., Bailey, T. R., Leng, M. J., & Abels, H. A., 2013. CO_2 drawdown following the middle Miocene expansion of the Antarctic Ice Sheet. Paleoceanography, 28(1), 42-53.

Bartoli, G., Hönisch, B., & Zeebe, R. E., 2011. Atmospheric CO_2 decline during the Pliocene intensification of Northern Hemisphere glaciations. Paleoceanography, 26(4).

Bertram, R. A., Wilson, D. J., van de Flierdt, T., McKay, R. M., Patterson, M. O., Jimenez-Espejo, F. J., ... & Riesselman, C. R., 2018. Pliocene deglacial event timelines and the biogeochemical response offshore Wilkes Subglacial Basin, East Antarctica. Earth and Planetary Science Letters, 494, 109-116.

Billups, K., & Schrag, D. P., 2003. Application of benthic foraminiferal Mg/Ca ratios to questions of Cenozoic climate change. Earth and Planetary Science Letters, 209(1-2), 181-195.

Bombard, S. E., Leckie, R. M., Browne, I. M., Shevenell, A. E., McKay, R. M., & Harwood, D. M., 2024. Miocene Climatic Optimum and Middle Miocene Climate Transition: a foraminiferal record from the central Ross Sea, Antarctica. Journal of Micropalaeontology, 43(2), 383-421.

Brancolini, G., Harris, P., 2000. Post Cruise Report AGSO Survey 217: Joint Italian/Australian Marine Geoscience Expedition Aboard the R.V. Tangaroa to the George Vth Land Region of East Antarctica during February–March, (2000). AGSO Record 2000/38.

Chorley, H., Levy, R., Naish, T., Lewis, A., Cox, S., Hemming, S., ... & Lurcock, P., 2023. East Antarctic Ice Sheet variability during the middle Miocene Climate Transition captured in drill cores from the Friis Hills, Transantarctic Mountains. Bulletin, 135(5-6), 1503-1529.

Close, D. I., Stagg, H. M. J., & O'Brien, P. E., 2007. Seismic stratigraphy and sediment distribution on the Wilkes Land and Terre Adélie margins, East Antarctica. Marine Geology, 239(1-2), 33-57.

Colleoni, F., De Santis, L., Naish, T. R., DeConto, R. M., Escutia, C., Stocchi, P., ... & Wilson, D. J., 2022. Past Antarctic ice sheet dynamics (PAIS) and implications for future sea-level change. In Antarctic climate evolution (pp. 689-768). Elsevier.

Colleoni, F., De Santis, L., Siddoway, C. S., Bergamasco, A., Golledge, N. R., Lohmann, G., ... & Siegert, M. J., 2018. Spatio-temporal variability of processes across Antarctic ice-bed–ocean interfaces. Nature Communications, 9(1), 2289.

Cook, C. P., Van De Flierdt, T., Williams, T., Hemming, S. R., Iwai, M., Kobayashi, M., ... & Yamane, M., 2013. Dynamic behaviour of the East Antarctic ice sheet during Pliocene warmth. Nature Geoscience, 6(9), 765-769.

Cooper, A. K., Barrett, P. J., Hinz, K., Traube, V., Letichenkov, G., & Stagg, H. M., 1991. Cenozoic prograding sequences of the Antarctic continental margin: a record of glacio-eustatic and tectonic events. Marine Geology, 102(1-4), 175-213.

Cramer, B. S., Miller, K. G., Barrett, P. J., & Wright, J. D., 2011. Late Cretaceous–Neogene trends in deep ocean temperature and continental ice volume: Reconciling records of benthic foraminiferal geochemistry (δ^{18}O and Mg/Ca) with sea level history. Journal of Geophysical Research: Oceans, 116(C12).

Crampton, J. S., Cody, R. D., Levy, R., Harwood, D., McKay, R., & Naish, T. R., 2016. Southern Ocean phytoplankton turnover in response to stepwise Antarctic cooling over the past 15 million years. Proceedings of the National Academy of Sciences, 113(25), 6868-6873.

Cui, T., & Margrave, G. F., 2015. Seismic-to-well ties by smooth dynamic time warping. CREWES Research Report, 27:1–26.

Cui, Y., Schubert, B. A., & Jahren, A. H., 2020. A 23 my record of low atmospheric CO_2. Geology, 48(9), 888-892.

De Boer, B., Van de Wal, R. S. W., Bintanja, R., Lourens, L. J., & Tuenter, E., 2010. Cenozoic global ice-volume and temperature simulations with 1-D ice-sheet models forced by benthic δ18O records. Annals of glaciology, 51(55), 23-33.

De Santis, L., Brancolini, G., and Donda, F., 2003. Seismo-stratigraphic analysis of the Wilkes Land continental margin (East Antarctica): influence of glacially driven processes on the Cenozoic deposition. Deep Sea Res. Part II, 50(8-9): 1563–1594.

Dickens, G. R., & Owen, R. M., 1999. The latest Miocene–early Pliocene biogenic bloom: a revised Indian Ocean perspective. Marine Geology, 161(1), 75-91.

Donda, F., Brancolini, G., De Santis, L., and Trincardi F., 2003. Seismic facies and sedimentary processes on the continental rise off Wilkes Land (East Antarctica): evidence of bottom current activity. Deep Sea Res., Part II, 50(8–9): 1509–1527.

Donda, F., Brancolini, G., O'Brien, P. E., De Santis, L., & Escutia, C., 2007. Sedimentary processes in the Wilkes Land margin: a record of the Cenozoic East Antarctic Ice Sheet evolution. Journal of the Geological Society, 164(1), 243-256.

Dorschel, B., Hehemann, L., Viquerat, S., Warnke, F., Dreutter, S., Tenberge, Y. S., ... & Arndt, J. E. 2022. The international bathymetric chart of the Southern Ocean version 2. Scientific Data, 9(1), 275.

Duncan, B., McKay, R., Levy, R., Naish, T., Prebble, J.G., Sangiorgi, F., Krishnan, S., Hoem, F., Clowes, C., Dunkley Jones, T., Gasson, E., Kraus, C., Kulhanek, D.K., Meyers, S.R., Moossen, H., Warren, C., Willmott, V., Ventura, G.T., Bendle, J., 2022. Climatic and tectonic drivers of late Oligocene Antarctic ice volume. Nat. Geosci. 1–7. https://doi.org/10.1038/s41561-022-01025-x

Escutia, C., Bárcena, M. A., Lucchi, R. G., Romero, O., Ballegeer, A. M., Gonzalez, J. J., & Harwood, D. M., 2009. Circum-Antarctic warming events between 4 and 3.5 Ma recorded in marine sediments from the Prydz Bay (ODP Leg 188) and the Antarctic Peninsula (ODP Leg 178) margins. Global and Planetary Change, 69(3), 170-184.

Escutia, C., Brinkhuis, H., & Klaus, A., 2011a. IODP Expedition 318: From greenhouse to icehouse at the Wilkes Land Antarctic margin. Scientific Drilling, 12, 15-23.

Escutia, C., Brinkhuis, H., and the Expedition 318 Science Party., 2014. From Greenhouse to Icehouse at the Wilkes Land Antarctic margin: IODP 318 synthesis of results. Developments in Marine Geology 7: 295-328. DOI: 10.1016/B978-0-444-62617-2.00012-8

Escutia, C., Brinkhuis, H., and the Expedition 318 Scientists, 2011b. Proc. IODP, 318: Tokyo (Integrated Ocean Drilling Program Management International, Inc.).

Escutia, C., De Santis, L., Donda, F., Dunbar, R. B., Cooper, A. K., Brancolini, G., & Eittreim, S. L., 2005. Cenozoic ice sheet history from East Antarctic Wilkes Land continental margin sediments. Global and Planetary Change, 45(1-3), 51-81.

Escutia, C., Eittreim, S. L., Cooper, A. K., & Nelson, C. H., 2000. Morphology and acoustic character of the Antarctic Wilkes Land turbidite systems: ice-sheet-sourced versus river-sourced fans. Journal of Sedimentary Research, 70(1), 84-93.

Escutia, C., Nelson, C.H., Acton, G.D., Eittreim, S.L., Cooper, A.K., Warnke, D.A., & Jaramillo, J.M. 2002. Current controlled deposition on the Wilkes Land continental rise, Antarctica. Geological Society, London, Memoirs, 22: 373-384. DOI: 10.1144/GSL.MEM. 2002.022.01.26.

Flower, B. P., & Kennett, J. P., 1994. The middle Miocene climatic transition: East Antarctic ice sheet development, deep ocean circulation and global carbon cycling. Palaeogeography, palaeoclimatology, palaeoecology, 108(3-4), 537-555.

Fogwill, C. J., Turney, C. S., Meissner, K. J., Golledge, N. R., Spence, P., Roberts, J. L., ... & Carter, L., 2014. Testing the sensitivity of the East Antarctic Ice Sheet to Southern Ocean dynamics: past changes and future implications. Journal of Quaternary Science, 29(1), 91-98.

Gei, D., Brancolini, G., De Santis, L., & Geletti, R. 2024., Well-log integration and seismic-to-well tie off George V Land (Antarctica). Geophysical Prospecting, 72(2), 685-704.

Golledge, N.R., Clark, P.U., He, F., Dutton, A., Turney, C.S.M., Fogwill, C.J., Naish, T.R., Levy, R.H., McKay, R.M., Lowry, D.P., Bertler, N.A.N., Dunbar, G.B., Carlson, A.E., 2021. Retreat of the Antarctic Ice Sheet During the Last Interglaciation and Implications for Future Change. Geophysical Research Letters 48. https://doi.org/10.1029/2021GL094513

Greenbaum, J. S., Blankenship, D. D., Young, D. A., Richter, T. G., Roberts, J. L., Aitken, A. R. A., ... & Siegert, M. J. 2015. Ocean access to a cavity beneath Totten Glacier in East Antarctica. Nature Geoscience, 8(4), 294-298.

Hartman, J. D., Sangiorgi, F., Salabarnada, A., Peterse, F., Houben, A. J., Schouten, S., ... & Bijl, P. K., 2018. Paleoceanography and ice sheet variability offshore Wilkes Land, Antarctica–Part 3: Insights from Oligocene–Miocene TEX 86-based sea surface temperature reconstructions. Climate of the Past, 14(9), 1275-1297. doi: 10.5194/cp-14-1275-2018

Haywood, A. M., & Valdes, P. J., 2004. Modelling Pliocene warmth: contribution of atmosphere, oceans and cryosphere. Earth and Planetary Science Letters, 218(3-4), 363-377.

Herbert, T. D., Lawrence, K. T., Tzanova, A., Peterson, L. C., Caballero-Gill, R., & Kelly, C. S., 2016. Late Miocene global cooling and the rise of modern ecosystems. Nature Geoscience, 9 (11), 843-847.

Holbourn, A., Kuhnt, W., Clemens, S., Prell, W., & Andersen, N., 2013. Middle to late Miocene stepwise climate cooling: Evidence from a high-resolution deep water isotope curve spanning 8 million years. Paleoceanography, 28(4), 688-699.

John, C. M., Karner, G. D., Browning, E., Leckie, R. M., Mateo, Z., Carson, B., & Lowery, C., 2011. Timing and magnitude of Miocene eustasy derived from the mixed siliciclastic-carbonate stratigraphic record of the northeastern Australian margin. Earth and Planetary Science Letters, 304(3-4), 455-467.

Khim, B. K., Song, B., Cho, H. G., Williams, T., Escutia, T., 2017. Late Neogene sediment properties in the Wilkes Land continental rise (IODP Exp. 318 Hole U1359A), East Antarctica.

Geosciences Journal, 21, 21-32.

Kominz, M. A., Miller, K. G., Browning, J. V., Katz, M. E., & Mountain, G. S., 2016. Miocene relative sea level on the New Jersey shallow continental shelf and coastal plain derived from one-dimensional backstripping: A case for both eustasy and epeirogeny. Geosphere, 12(5), 1437-1456.

Kuhnert, H., Bickert, T., & Paulsen, H., 2009. Southern Ocean frontal system changes precede Antarctic ice sheet growth during the middle Miocene. Earth and Planetary Science Letters, 284(3-4), 630-638.

Lear, C. H., Coxall, H. K., Foster, G. L., Lunt, D. J., Mawbey, E. M., Rosenthal, Y., ... & Wilson, P. A., 2015. Neogene ice volume and ocean temperatures: Insights from infaunal foraminiferal Mg/Ca paleothermometry. Paleoceanography, 30(11), 1437-1454.

Levy, R. H., Dolan, A. M., Escutia, C., Gasson, E. G., McKay, R. M., Naish, T., ... & Verret, M., 2022. Antarctic environmental change and ice sheet evolution through the Miocene to Pliocene–a perspective from the Ross Sea and George V to Wilkes Land Coasts. In Antarctic Climate Evolution (pp. 389-521). Elsevier.

Levy, R. H., Harwood, D., Florindo, F., Sangiorgi, F., Tripati, R., Von Eynatten, H., ... & SMS Science Team., 2016. Antarctic ice sheet sensitivity to atmospheric CO_2 variations in the early to mid-Miocene. Proceedings of the National Academy of Sciences, 113(13), 3453-3458.

Lewis, A. R., Marchant, D. R., Ashworth, A. C., Hemming, S. R., & Machlus, M. L. 2007. Major middle Miocene global climate change: Evidence from East Antarctica and the Transantarctic Mountains. Geological Society of America Bulletin, 119(11-12), 1449-1461.

Lunt, D. J., Haywood, A. M., Schmidt, G. A., Salzmann, U., Valdes, P. J., & Dowsett, H. J., 2010. Earth system sensitivity inferred from Pliocene modelling and data. Nature Geoscience, 3(1), 60-64.

Marschalek, J. W., Zurli, L., Talarico, F., Van de Flierdt, T., Vermeesch, P., Carter, A., ... & McKay, R. M., 2021. A large West Antarctic Ice Sheet explains early Neogene sea-level amplitude. Nature, 600(7889), 450-455.

Martínez-Botí, M. A., Foster, G. L., Chalk, T. B., Rohling, E. J., Sexton, P. F., Lunt, D. J., ... & Schmidt, D. N., 2015. Plio-Pleistocene climate sensitivity evaluated using high-resolution CO_2 records. Nature, 518(7537), 49-54.

McKay, R. M., Escutia, C., De Santis, L., Donda, F., Duncan, B., Gohl, K., ... & Williams, T. (2022). Cenozoic history of Antarctic glaciation and climate from onshore and offshore studies. In Antarctic climate evolution (pp. 41-164). Elsevier.

McKay, R., Cockrell, J., Shevenell, A. E., Laberg, J. S., Burns, J., Patterson, M., ... & IODP Expedition 374 Science Team., 2025. Miocene ice sheet dynamics and sediment deposition in the central Ross Sea, Antarctica. Geological Society of America Bulletin, 137(3-4), 1267-1291.

Miller, K. G., Browning, J. V., Schmelz, W. J., Kopp, R. E., Mountain, G. S., & Wright, J. D., 2020. Cenozoic sea-level and cryospheric evolution from deep-sea geochemical and continental margin records. Science advances, 6(20).

Modestou, S. E., Leutert, T. J., Fernandez, A., Lear, C. H., & Meckler, A. N., 2020. Warm middle Miocene Indian Ocean bottom water temperatures: Comparison of clumped isotope and Mg/Ca-based estimates. Paleoceanography and Paleoclimatology, 35(11), e2020PA003927.

Morlighem, M., Rignot, E., Binder, T., Blankenship, D., Drews, R., Eagles, G., ... & Young, D. A., 2020. Deep glacial troughs and stabilizing ridges unveiled beneath the margins of the Antarctic ice sheet. Nature geoscience, 13(2), 132-137.

Mudelsee, M., & Raymo, M. E., 2005. Slow dynamics of the Northern Hemisphere glaciation. Paleoceanography, 20(4).

Orejola, N., Passchier, S., & Expedition, IODP., 2014. Sedimentology of lower Pliocene to upper Pleistocene diamictons from IODP site U1358, Wilkes Land margin, and implications for East Antarctic Ice Sheet dynamics. Antarctic Science, 26(2), 183-192.

Patterson, M.O., McKay, R., Naish, T., Escutia, C., Jimenez-Espejo, F.J., Raymo, M.E., et al.,

2014. Orbital forcing of the East Antarctic ice sheet during the Pliocene and Early Pleistocene. Nature Geoscience 7 (11), 841-847.

Paxman, G. J., Gasson, E. G., Jamieson, S. S., Bentley, M. J., & Ferraccioli, F., 2020. Long-term increase in Antarctic Ice Sheet vulnerability driven by bed topography evolution. Geophysical Research Letters, 47(20).

Pérez, L. F., McKay, R. M., De Santis, L., Larter, R. D., Levy, R. H., Naish, T. R., ... & Speece, M., 2022. Early to middle Miocene ice sheet dynamics in the westernmost Ross Sea (Antarctica): regional correlations. Global and Planetary Change, 216, 103891.

Pierce, E. L., van de Flierdt, T., Williams, T., Hemming, S. R., Cook, C. P., & Passchier, S., 2017. Evidence for a dynamic East Antarctic ice sheet during the mid-Miocene climate transition. Earth and Planetary Science Letters, 478, 1-13.

Pillot, Q., Suchéras-Marx, B., Sarr, A. C., Bolton, C. T., & Donnadieu, Y., 2023. A global reassessment of the spatial and temporal expression of the Late Miocene Biogenic Bloom. Paleoceanography and Paleoclimatology, 38(3), e2022PA004564.

Pollard, D., DeConto, R. M., & Alley, R. B. (2015). Potential Antarctic Ice Sheet retreat driven by hydrofracturing and ice cliff failure.Earth and Planetary Science Letters, 412, 112-121.

Prentice, M. L., & Matthews, R. K., 1991. Tertiary ice sheet dynamics: The snow gun hypothesis. Journal of Geophysical Research: Solid Earth, 96(B4), 6811-6827.

Pritchard, H., Ligtenberg, S. R., Fricker, H. A., Vaughan, D. G., van den Broeke, M. R., & Padman, L., 2012. Antarctic ice-sheet loss driven by basal melting of ice shelves. Nature, 484(7395), 502-505.

Raymo, M. E., Grant, B., Horowitz, M., & Rau, G. H., 1996. Mid-Pliocene warmth: stronger greenhouse and stronger conveyor. Marine Micropaleontology, 27(1-4), 313-326.

Reinardy, B. T., Escutia, C., Iwai, M., Jimenez-Espejo, F. J., Cook, C., van de Flierdt, T., & Brinkhuis, H., 2015. Repeated advance and retreat of the East Antarctic Ice Sheet on the continental shelf during the early Pliocene warm period. Palaeogeography, Palaeoclimatology, Palaeoecology, 422, 65-84.

Salabarnada, A., Escutia, C., Röhl, U., Nelson, C. H., McKay, R., Jiménez-Espejo, F. J., ... & Brinkhuis, H., (2018). Paleoceanography and ice sheet variability offshore Wilkes Land, Antarctica–Part 1: Insights from late Oligocene astronomically paced contourite sedimentation. Climate of the Past, 14(7), 991-1014. DOI:10.5194/cp-14-991-2018

Salzmann, U., Williams, M., Haywood, A. M., Johnson, A. L., Kender, S., & Zalasiewicz, J., 2011. Climate and environment of a Pliocene warm world. Palaeogeography, Palaeoclimatology, Palaeoecology, 309(1-2), 1-8.

Sangiorgi, F., Bijl, P. K., Passchier, S., Salzmann, U., Schouten, S., McKay, R., ... & Brinkhuis, H., 2018. Southern Ocean warming and Wilkes Land ice sheet retreat during the mid-Miocene. Nature communications, 9(1), 317.

Shevenell, A. E., Kennett, J. P., & Lea, D. W., 2004. Middle Miocene Southern Ocean cooling and Antarctic cryosphere expansion. Science, 305(5691), 1766-1770.

Shevenell, A. E., Kennett, J. P., & Lea, D. W., 2008. Middle Miocene ice sheet dynamics, deep-sea temperatures, and carbon cycling: A Southern Ocean perspective. Geochemistry, Geophysics, Geosystems, 9(2).

Siegert, M., & Golledge, N. R., 2022. Advances in numerical modelling of the Antarctic ice sheet. In Antarctic Climate Evolution (pp. 199-218). Elsevier.

Sosdian, S. M., Greenop, R., Hain, M. P., Foster, G. L., Pearson, P. N., & Lear, C. H., 2018. Constraining the evolution of Neogene ocean carbonate chemistry using the boron isotope pH proxy. Earth and Planetary Science Letters, 498, 362-376.

Steinthorsdottir, M., Coxall, H. K., De Boer, A. M., Huber, M., Barbolini, N., Bradshaw, C. D., ... & Strömberg, C. A. E., 2021. The Miocene: The future of the past. Paleoceanography and Paleoclimatology, 36(4), e2020PA004037.

Tauxe, L., Stickley, C. E., Sugisaki, S., Bijl, P. K., Bohaty, S. M., Brinkhuis, H., Escutia, C., Flores, J. A., Houben, A., Iwai, M., et al., 2012. Chronostratigraphic framework for the IODP expedition 318 cores from the Wilkes Land margin: Constraints for paleoceanographic reconstruction. Paleoceanography, 27(2).

Taylor-Silva, B. I., & Riesselman, C. R., 2018. Polar frontal migration in the warm late Pliocene: Diatom evidence from the Wilkes Land margin, East Antarctica. Paleoceanography and Paleoclimatology, 33(1), 76-92.

Verducci, M., Foresi, L. M., Scott, G. H., Sprovieri, M., Lirer, F., & Pelosi, N., 2009. The Middle Miocene climatic transition in the Southern Ocean: evidence of paleoclimatic and hydrographic changes at Kerguelen plateau from planktonic foraminifers and stable isotopes. Palaeogeography, Palaeoclimatology, Palaeoecology, 280(3-4), 371-386.

Wen, Y., Zhang, L., Holbourn, A. E., Zhu, C., Huntington, K. W., Jin, T., ... & Wang, C., 2023. CO_2-forced Late Miocene cooling and ecosystem reorganizations in East Asia. Proceedings of the National Academy of Sciences, 120(5).

Westerhold, T., Marwan, N., Drury, A. J., Liebrand, D., Agnini, C., Anagnostou, E., ... & Zachos, J. C., 2020. An astronomically dated record of Earth’s climate and its predictability over the last 66 million years. Science, 369(6509), 1383-1387.

Whitehead, J. M., & Bohaty, S. M., 2003. Pliocene summer sea surface temperature reconstruction using silicoflagellates from Southern Ocean ODP Site 1165. Paleoceanography, 18(3).

Yilmaz, Ö., 2001. Seismic data processing. Tulsa, OK: Society of Exploration Geophysicists.

Zachos, J., Pagani, M., Sloan, L., Thomas, E., & Billups, K., 2001. Trends, rhythms, and aberrations in global climate 65 Ma to present Science, 292(5517), 686-693.

Zhang, Y. G., Pagani, M., Liu, Z., Bohaty, S. M., & DeConto, R., 2013. A 40-million-year history of atmospheric CO_2. Philosophical Transactions: Mathematical, Physical and Engineering Sciences,

Figure Caption

Fig. 1 The study area and the location of the IODP 318 sites with the seismic profiles mentioned in the text. The position of Site U1356 is located outside the map (about 400 km to the west). Bathymetric data were taken from IBCSOv2 (Dorschel et al., 2022), and the WSB topography in the inset map is isostatically corrected (Paxmann et al., 2020). The thin red arrow represents the course of the channels on the continental rise, while the thick red arrow shows the most recent flow of the ice stream on the continental shelf (McMullen et al., 2005).

Fig. 2 Seismic profile through IODP sites U1359 and U1361. The seismic sections in Fig. 2a are from a standard processing with window balancing to better represent the base of the channel shallow water system and the sediment wave field. Fig. 2b is the same line as 2a, 2c and 2d, but has been processed and shown in true amplitude to show the HASP. The base of the channel-levee system is younger northward, from WL-U5 to WL-U6. Note that the HASP began with WL-U7, but developed more broadly after WL-U7a

Fig. 3 Velocity and density logs for Sites U1359 and U1361, derived from the integration of wire and core log data. The high variability of the acoustic impedance and reflection coefficients, consistent with the HASP, depends mainly on the high variability of the density log. The synthetic trace (green seismogram) was obtained by convolving the reflection coefficient with the wavelet extracted from the seafloor and shows a remarkable similarity with the real trace (red seismogram).

Fig. 4 (a) Biogenic opal, (b) NGR, (c) density, (d) diatom content based on the logs integration at Sites U1359 and U1361. In red the data from WRMSL, blue from wireline logs.

Fig. 5 Depositional rates and temporal assessment of seismic unconformities at Sites U1359 and U1361, based on the paleomagnetic tie points of Tauxe et al. (2012). Deviating from Tauxe et al. (2012), we introduce a non-depositional hiatus at WL-U7 for Site U1359**.**

Fig. 6 Seismic sequences and main climatic events of the Neogene. Benthic δ^{18}O (blue) and δ^{13}C (green) from Westerhold et al. (2020); global mean bottom temperature from Westerhold et al. (2020), (black) and Cramer et al. (2011) Eq. 7a (green) and Eq. 7b (magenta), sea level curves from Miller et al., 2020 (green), Kominz et al., 2016 (magenta); John et al., 2011 (black).

Fig. 7 The shelf margin: a) Seismic line WEGA-21, which is perpendicular to the margin, shows the alternation between type IIA and IA seismic sequences in the early Pliocene. b) Seismic line ATC82-118, which is parallel to the shelf margin, shows that the canyons that fed the channel dam during the Neogene were buried by the advancing shelf margin fan with seismic sequence IA.

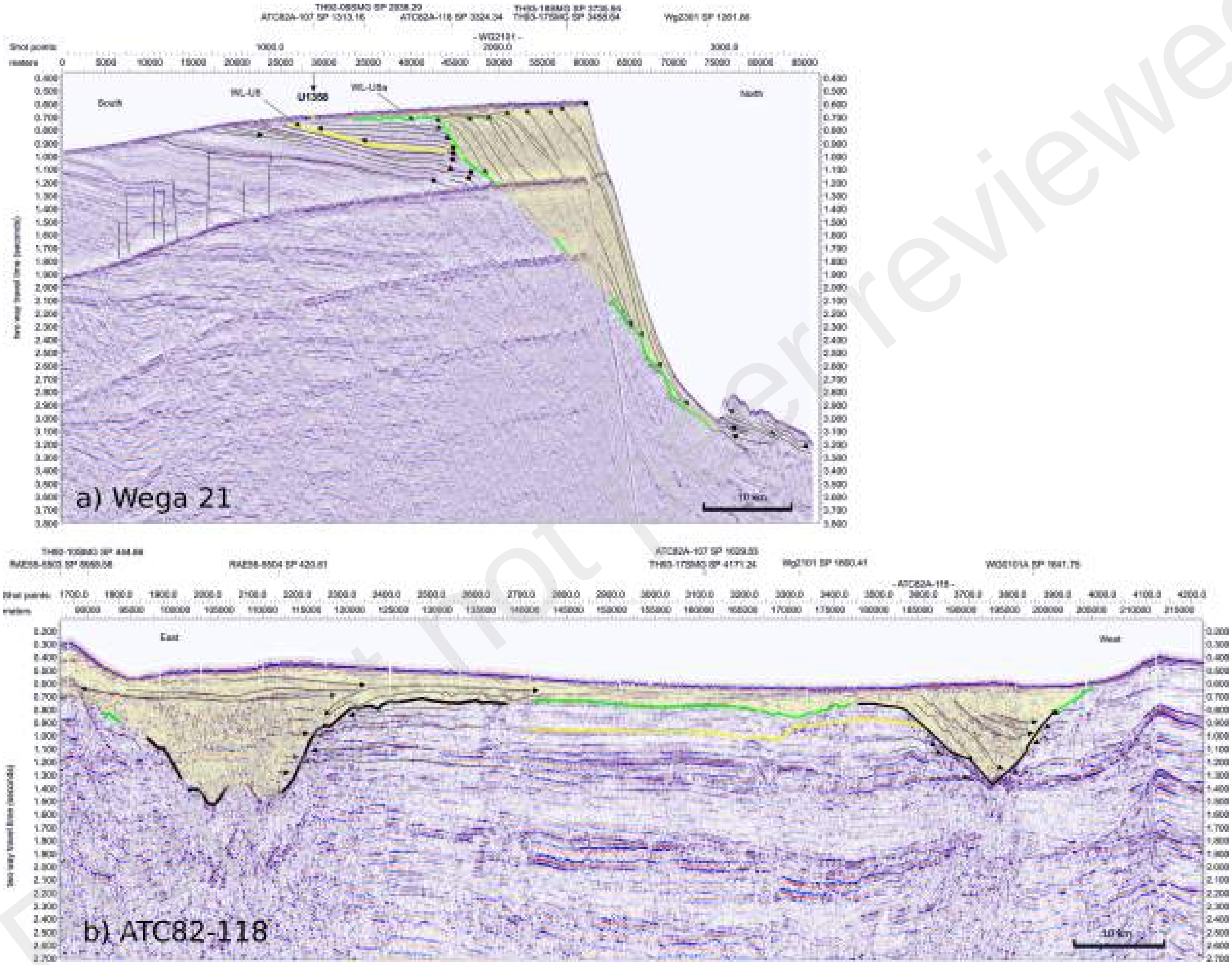
TH90-058MG SP 2838.20
ATC82A-107 SP 1313.16
ATC82A-118 SP 3324.34
TH93-168MG SP 3726.84
TH93-175MG SP 3458.04
Wg2301 SP 1201.86
- WG2101 -
Shot points
meters
South
WL-U8
U1358
WL-U8a
North
two way travel time (seconds)
10 km
a) Wega 21
TH93-105MG SP 444.88
RAE56-5503 SP 6560.58
RAE56-5504 SP 420.61
ATC82A-107 SP 1629.03
TH93-175MG SP 4171.24
Wg2101 SP 1660.41
WG0101A SP 1641.75
- ATC82A-118 -
Shot points
meters
East
West
two way travel time (seconds)
10 km
b) ATC82-118